

# Optical system for an astrometric survey from space

James D. Phillips and Robert D. Reasenberg\*

Smithsonian Astrophysical Observatory  
Harvard-Smithsonian Center for Astrophysics  
MS63, 60 Garden St., Cambridge, MA 02138

## ABSTRACT

We present an optical design for a spaceborne instrument, of about  $\frac{1}{2}$  m aperture, to perform a combined astrometric and photometric survey *via* a scan similar to that of Hipparcos. A CCD detector array with Time Delayed Integration will permit an astrometric mission accuracy better than 50 microarcseconds for stars brighter than 10th magnitude,  $1\frac{1}{2}$  orders better than Hipparcos. The passband is nominally 0.4 to 0.9 microns. For the instrument to have both high measurement rate and high accuracy, the optical system must satisfy several requirements. It should have aberration well under diffraction, for high precision in centroiding and as a means of keeping unmodeled shifts of the image centroids small. The system should have a *wide* field of view so that there is a large overlap of successive scans, have a *large* field of view for scientific throughput (sum over targets of the inverse variance), and have low image distortion so that the stellar images move at constant rate along columns of detector pixels. The design presented meets these requirements using aspheric surfaces that are manufacturable. We have demonstrated that the instrument will determine the temperature of an observed star without requiring a dispersive element or color filters. The design is thus free of transmissive elements, and protected from the systematic errors that they might have induced, e.g., due to thermal variation and to chromatic effects.

This study was inspired by our previous consideration of scientific throughput. Our study of data reduction from a scanning astrometric survey mission demonstrated that there is a substantial gain in mission accuracy if the spacecraft precesses without discontinuities such as those that result from gas jet firings. Our study of methods of precessing the spacecraft showed that smooth rotation would be possible using solar radiation pressure, but only if the spacecraft rotation rate were increased. Maintaining the integration time for each object would require an optical design of shorter focal length. Meanwhile, our study of mission accuracy as a function of focal length showed that another increase of accuracy would result from shorter focal length, *via* the greater number of lower-accuracy measurements. Therefore we performed this optical study to find a design with shorter focal length, having a proportionate increase in field of view. We conceived and investigated a family of short focal length, wide-field designs, and developed a methodology to facilitate selection from among them. The new baseline design achieves diffraction-limited images over a  $2.2^\circ$  FOV with a  $1.1^\circ$  square central blockage, and has a 7.5 m focal length.

**Keywords:** Astrometry, space, instrument, optical design, estimation

## 1. INTRODUCTION

The Fast Astrometric Mapping Explorer (FAME-98)<sup>a</sup> is a mission concept for a spaceborne instrument that would perform a high-precision astrometric survey, and may also perform multichannel photometry. The design objectives, which have been

\* Further author information:

JDP: phone, 617-495-7360 (fax 7109), [jphillips@cfa.harvard.edu](mailto:jphillips@cfa.harvard.edu) RDR: phone, 617-495-7108 (fax 7109), [reasenberg@cfa.harvard.edu](mailto:reasenberg@cfa.harvard.edu)

<sup>a</sup> FAME-98 should not be confused with the Fizeau Astrometric Mapping Explorer (FAME), which was the subject of an unsuccessful JPL-USNO MIDEX proposal in December, 1995. This proposal contains an optical diagram, but no optical prescription. The optical diagram was quite different from that discussed here. For clarity, we refer to the Fizeau Astrometric Mapping Explorer, including its optical design, as FAME-95, to the SAO design with  $0.75^\circ$  dia. field of view and 36 m focal length as FAME-96, and to the current nominal design for the Fast Astrometric Mapping Explorer with  $2.2^\circ$  dia. field of view and 7.5 m focal length, spelled out in this paper and its companion (reference 2), as FAME-98.

met in this study, are to be able to measure  $10^7$  stars over the full sky, with an accuracy of 0.05 mas for mag < 9 and 20 mas for mag 15. The satellite will spin continuously, scanning the stellar images across the detector. The collected charge will be shifted along CCD columns, so that charge packets will follow the corresponding images, gaining charge as they cross a detector chip.

A preliminary optical design called FAME-96 was created at SAO in Oct.-Nov. 1996. This design, which was inspired by Høg, *et al.*,<sup>1</sup> achieved diffraction-limited images over a  $0.75^\circ$  diameter field of view with a 36 m focal length. Our recent studies have shown that *mission accuracy*, i.e., the accuracy after all observations have been analyzed, could be improved by shortening the focal length while keeping the field of view large enough to accommodate the full focal-plane array. Mission accuracy is increased by a factor of two if the telescope focal length is shortened by a factor of six. Greater improvements are possible with focal lengths as short as 3.75 m,<sup>2</sup> although the optics for this focal length may be difficult. With the shorter focal length, each pixel maps to a larger region of sky. The enhanced throughput comes from the much larger number of star measurements, even though each measurement is less precise. Independent of the increased throughput, there are strong reasons for considering a shorter focal length. Holding fixed the time a star takes to cross a CCD, the spacecraft spin rate is inversely proportional to focal length. Higher spin rate facilitates the use of solar radiation instead of gas jet firings to drive the precession, so arcs of unbroken data are longer. This substantially improves the internal coherence of the data reduction, and thereby improves mission accuracy.

The shorter focal length creates an optical design challenge, however. To keep the detector area constant, the angular diameter of the field of view must be increased in inverse proportion to the focal length. A new shorter-focal-length design, called FAME-98, has been created for the instrument. In this paper, we discuss a family of optical designs for FAME-98 that achieve the required range of focal lengths and field of view areas. They differ in these and other properties, and we present a method for selecting from among them.

A previous study has shown, surprisingly, that if the aperture is rectangular, mission accuracy depends only on the product of its width and height.<sup>2</sup> This comes about because an aperture elongated in the scan direction reduces the angular size of the diffraction pattern, requiring the angular extent of a detector pixel to be small in order to make use of the fine diffraction pattern. With a fixed degree of anamorphism, a greater number of pixels is then "wasted" between stars. In this study, the aperture has been made square because that may simplify packaging. The aperture is divided by the complex mirror into two stripes, in this study 0.5 m in the scan direction (the direction of motion of the look direction) by 0.25 m in cross-scan.

Before developing the systematic approach described here, we found many solutions that met some of the requirements. The requirements, however, are not rigid: trading among them by adjusting optical design parameters may yield a benefit in scientific throughput or cost. A superior approach, at least at this conceptual stage, is to present a set of designs that allow a trade among blur, overall length, and field blockage. (The last of these pertains to the particular technique used to achieve beam clearance in this family of designs.) Keeping track of all three while moving on an *ad hoc* path in parameter space proved difficult, and the approach, slow. Therefore, we developed a technique for making a map on which the trades could be visualized easily.

## 2. REQUIREMENTS UPON OPTICAL SYSTEM

High accuracy astrometry places the following seven requirements on the optical design (summarized in Table 1):

- a) The design must be diffraction-limited, in order not to degrade precision.
- b) Shifts of the centroid due to mechanical changes in the optics and to uneven changes of reflectivity must be kept to a minimum, and keeping geometrical aberration low may aid in this. This hypothesis has not yet been investigated.
- c) The analysis of the astrometric data is envisioned to occur in three stages: (A) creation of a rotation model for the instrument over one "observing spiral" (of duration ~1 day); (B) a global fit, connecting all observing spirals; and (C) the application of the spiral and global models to each star observed so as to create a catalog.<sup>2</sup> The coherence of the stage A analysis improves substantially when the field of view is widened, giving more overlap of the patches of sky covered on successive rotations.

**Table 1.** Requirements.

Requirement	Optical condition	Criterion
a) High-precision centroiding	Aberration < diffraction	rms blur < 1/3 $\lambda_0/S$
b) High-accuracy centroiding	Unmodeled shifts << diffraction	not yet known
c) Large track-to-track overlap (facilitates data reduction)	Wide field of view (cross-scan)	not yet known
d) Scientific throughput	Large field of view (area)	22 2K×4K CCD's; 15 $\mu\text{m}$ pixels.
e) Images move at constant speed	Image distortion rms shift < $\lambda_0/(10S)$	0.02%
f) Packaging	Overall length, after any folding	Length < 2 m
g) Pixel size appropriate to point spread function	pixels per Airy box ( $n_s$ , Eq. 3)	$n_s \approx 0.8$ to 1.6 (see Eq. 3)

**d)** Scientific throughput demands a large field of view, but cost constrains the area of detector (CCD's) that can be employed<sup>b</sup>. This optical study assumes a constant detector area and physical pixel size. With a focal length  $f$ , the area of sky covered at one time is

$$\Omega = \frac{N_{\text{CCD}} N_s N_c w^2}{f^2} = \left( \frac{7.5 \text{ m}}{f} \right)^2 2.42 \text{ sq. deg.} \quad (1)$$

where  $N_{\text{CCD}}$  is the number of CCD chips,  $N_s$  and  $N_c$  are the number of pixels of each CCD in the scan and cross-scan directions, respectively, and  $w$  is the pixel size (the pixels are taken to be square). The angular radius of the field of view required to accommodate these detectors in a fully-filled circle is

$$\theta = \left( \frac{7.5 \text{ m}}{f} \right) (0.88^\circ) . \quad (2)$$

However, the packing will not be so efficient, and there is likely to be a substantial central field blockage, so the requirement for the radius of the field of view was taken in this study to be 25% larger.

**e)** A requirement particular to astrometry with a scanning instrument is that image distortion be low in order that stellar images move down a single column of pixels. Furthermore, the images must move at constant speed so that the accumulating charge packet moves with the image – the charge must not be smeared out along the column. The latter condition results in a somewhat more stringent requirement. The motion along the column should not vary from motion at the best-fit constant speed<sup>c</sup> by more than about 1/3 of the rms half-width of the diffraction-limited image, about  $\lambda_0/(10S)$ . The designs considered herein are axisymmetric, so distortion is purely radial. Consider the nominal CCD and optical system of this paper, with a  $2.2^\circ$  diameter field of view and 7.5 m focal length, and a cubic distortion that shifts the image at the edge of the field by a fraction  $\alpha$  of the field radius. The variation of image speed is greatest for an image whose path goes through the center of the field. The above criterion implies  $\alpha < 0.02\%$ . The rms transverse image motion with respect to the best-fitting straight line<sup>d</sup> is greatest for an image that would just go through the edge of the field. The rms motion is less than half of the greatest along-column variation, and will likely be completely overshadowed by transverse motion due to spacecraft precession.

<sup>b</sup> For a given area of CCD, cost is relatively unaffected by choice of pixel size and shape, above a minimum achievable size. Sensitivity (for bright stars) increases with smaller pixels.

<sup>c</sup> Setting the clock speed of each detector chip independently will allow correction for different average image speeds at each chip. Then, only acceleration of the image while on the chip will cause smear.

<sup>d</sup> The chip can be rotated so as to be aligned with the best-fit linear trajectory, although this is probably unnecessary because of the larger, unavoidable, transverse motion due to spacecraft precession.

f) For this study, it was assumed that the instrument must fit within a cylinder of 2 m diameter, with axis parallel to the spin axis. The maximum spacing between optical elements was taken to be 1.8 m. By choosing a different point on the maps described below, we can accommodate smaller sizes, or take advantage of larger ones.

g) Finally, as mentioned above, the angular size of a pixel on the sky should be chosen to maximize sensitivity for the mix of targets of interest. Let  $n_s$  be the number of pixels per Airy box, where we define the width of an Airy box as the space between dark bands of the diffraction pattern of the rectangular aperture (ignoring the central obscuration). Let  $f$  be the effective focal length (EFFL),  $\lambda_o$  be the effective wavelength (0.6  $\mu\text{m}$ ), and  $S$  be the aperture width in the sensitive (scan) direction. Then

$$n_s = \frac{2f\lambda_o}{wS}. \quad (3)$$

A large value for  $n_s$  gives high precision for the observation. However, the area of sky covered (with constant detector area) scales as  $n_s^{-2}$ . A narrowly defined optimum value for  $n_s$  is found from Fig. 1 to be 0.6. However, the best value to use for the mission, considering precision as well as other factors, is still under study. The range of focal lengths covered in this study, 5 to 10 m, corresponds to  $n_s$  from 0.8 to 1.6. In FAME-95 and FAME-96,  $n_s$  was 4.8. Different EFFL values can be obtained by repeating the map-making procedure described below.

## 2.1. On-board centroiding.

Photon counts (charge measurements) from a group of pixels will be processed to produce an estimate of star position. The star's angle and amplitude (magnitude) must both be estimated, and because of the wavelength dependence of diffraction, the spectrum must also be estimated, or an *a priori* value used. To first order, it suffices to know the temperature of an equivalent black body. An error in the spectrum would cause a bias in position for a star not centered on a pixel or a pixel edge (although this bias would tend to average out for a large number of separate measurements of a given star).

We expected that when  $n_s$  is high (i.e., many pixels across the Airy box) the distribution of light on the detector would support the simultaneous estimation of position, brightness, and temperature. We expected a degradation at smaller  $n_s$ . We have performed a covariance study to determine the value of  $n_s$  at which that degradation became significant. We calculated the integral over wavelength of photon density for a rectangular aperture as a function of position on the detector, taking account of diffraction but neglecting aberration. We also calculated derivatives of photon density with respect to angle, amplitude, and temperature. (We modeled the spectrum as being from a black body. We see no reason why the estimation would not work with a more detailed single-parameter model of the spectrum, and with aberration included.) We then integrated these quantities over each pixel, for a number of choices of focal length and phase of the pixels with respect to the center of the stellar image. Enough pixels were included to cover several fringes near the center of the diffraction pattern. We then performed a weighted-least-squares fit to one of two models. In the first case, there was only one free parameter,  $p$ , the position of the star in the scan direction. In the second case, two additional parameters were fit, the temperature of the star and its brightness. In both cases, for small values of  $n_s$ , the formal single-measurement angle uncertainty,  $\sigma(p)$ , was found to depend on the phase of the star, i.e., its position with respect to the pixel boundary. Parameter uncertainties were determined by taking an average of information (which is the inverse square of uncertainty) over that phase.

The results of the analysis are given in Fig.1. The quantities plotted,  $\sigma_M(x) = n_s\sigma(x)$ , where  $x = \{\text{angle, magnitude, temperature}\}$ , reflect the dependence of information (i.e., number of measurements) on  $n_s$ : sky coverage is proportional to  $n_s^{-2}$ , therefore information is, so  $\sigma_M$  (standard deviation based on all mission data) is proportional to  $n_s$ . Single-measurement uncertainties for angle, magnitude, and temperature, for a  $V=9.1$  star with  $n_s=1.2$ , are 0.57 milliarcsec, 0.0026 mag, and 48 K, respectively.

The expected degradation in  $\sigma_M(p)$  due to the need to fit 3 parameters does occur, but, perhaps surprisingly, only for  $n_s < 0.6$ , i.e.,  $f < 3.75$  m and when 1.7 Airy boxes fit within a pixel. This degradation is visible in the figure, in the upper panel, as the increase of the error for a 3-parameter fit (line) over that for a 1-parameter fit (dots). Therefore, requiring that temperature be determined from the FAME data does not prevent a substantial increase of sensitivity over an instrument employing  $n_s = 4.8$ ; in fact the lower limit to  $n_s$  is still set by the need to create an optical system with sufficiently short focal length and wide field of view.

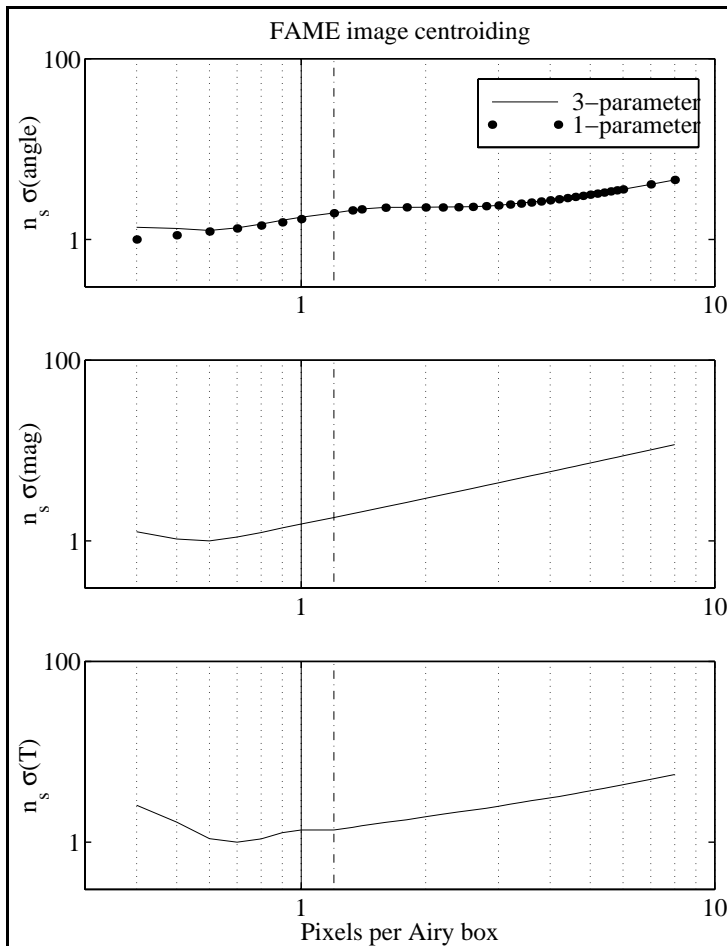


**Figure 1.** Formal uncertainty of angle, amplitude, and temperature (arbitrary scale). Ordinates are multiplied by  $n_s$  to reflect dependence of mission accuracy on pixel size. Dash-dot lines are at  $n_s = 1.2$ . Single-measurement uncertainties for angle, magnitude, and temperature, for a  $V=9.1$  star with  $n_s=1.2$ , are 0.57 milliarcsec, 0.0026 mag, and 48 K, respectively.

experimentation, is shown in Fig.2. The primary and secondary act as an ordinary Cassegrain, having a focal length somewhat less than the required overall focal length, and producing an image in the vicinity of the primary (dashed line in the figure). The concave tertiary magnifies this image to the final size and EFFL.

One might also consider an off-axis system, which could alleviate the significant beam blockage problems of this centered system. To employ off-axis systems for astrometry, however, one would have to establish that the lack of symmetry did not increase systematic error unacceptably, which requires a detailed understanding of the instrument thermal environment and the mounting of the optics, so consideration of them has been deferred.

The telescope is to be preceded by a Hipparcos-style "complex mirror:" two plane mirrors, one for each half of the aperture, maintained at a stable angle with respect to each other<sup>3</sup> (Fig. 2). The complex mirror is probably the place to put the aperture stop: it is the element most exposed to the outside. Variation of the temperature of that outside environment at the spacecraft spin rate is strongly suppressed by virtue of the solar shield, which is flat (or nearly so) and may be insulated, but there are small unavoidable perturbations such as the Earth crossing the aperture.<sup>6</sup> Therefore the complex mirror is

<sup>6</sup> The Earth subtends  $7.3^\circ$  from the intended 100,000 km altitude and, at 3 revolutions per hour, crosses a given direction in 24 sec.

The central panel of Fig. 1 shows a linear dependence of  $n_s \sigma(\text{mag})$  on  $n_s$ , i.e.,  $\sigma(\text{mag})$  is independent of  $n_s$  for  $n_s$  greater than about 0.6. The bottom panel shows that temperature is well-determined for all  $n_s$  for which calculations were performed. All three parameters show a loss of accuracy for small  $n_s$ ; for temperature, there is the greatest loss. The low uncertainties indicate that adequate spectral information is available without a prism. However, for smaller  $n_s$ , accuracy suffers: it is necessary to have signal in several pixels to be able to separate angle, amplitude, and temperature.

### 3. GENERAL DESIGN FORM

A number of general design forms were considered for FAME-98. It was decided early to investigate systems with the minimum number of powered mirrors as a likely means of minimizing complexity and cost. Systems having two elements with optical power ("two-mirror systems") did not have enough degrees of freedom to meet the criteria. In systems with three and more mirrors, it becomes increasingly complicated to keep optical elements from blocking light traveling between other elements. The scheme adopted for achieving beam clearance becomes a central part of the design, which multiplies the number of design forms that must be considered. Meanwhile, beam blockage sharply limits the number that are useful. Refractive elements might substantially improve performance, but represent a potential source of systematic error. Consideration of them has been postponed.

The design form chosen, after some

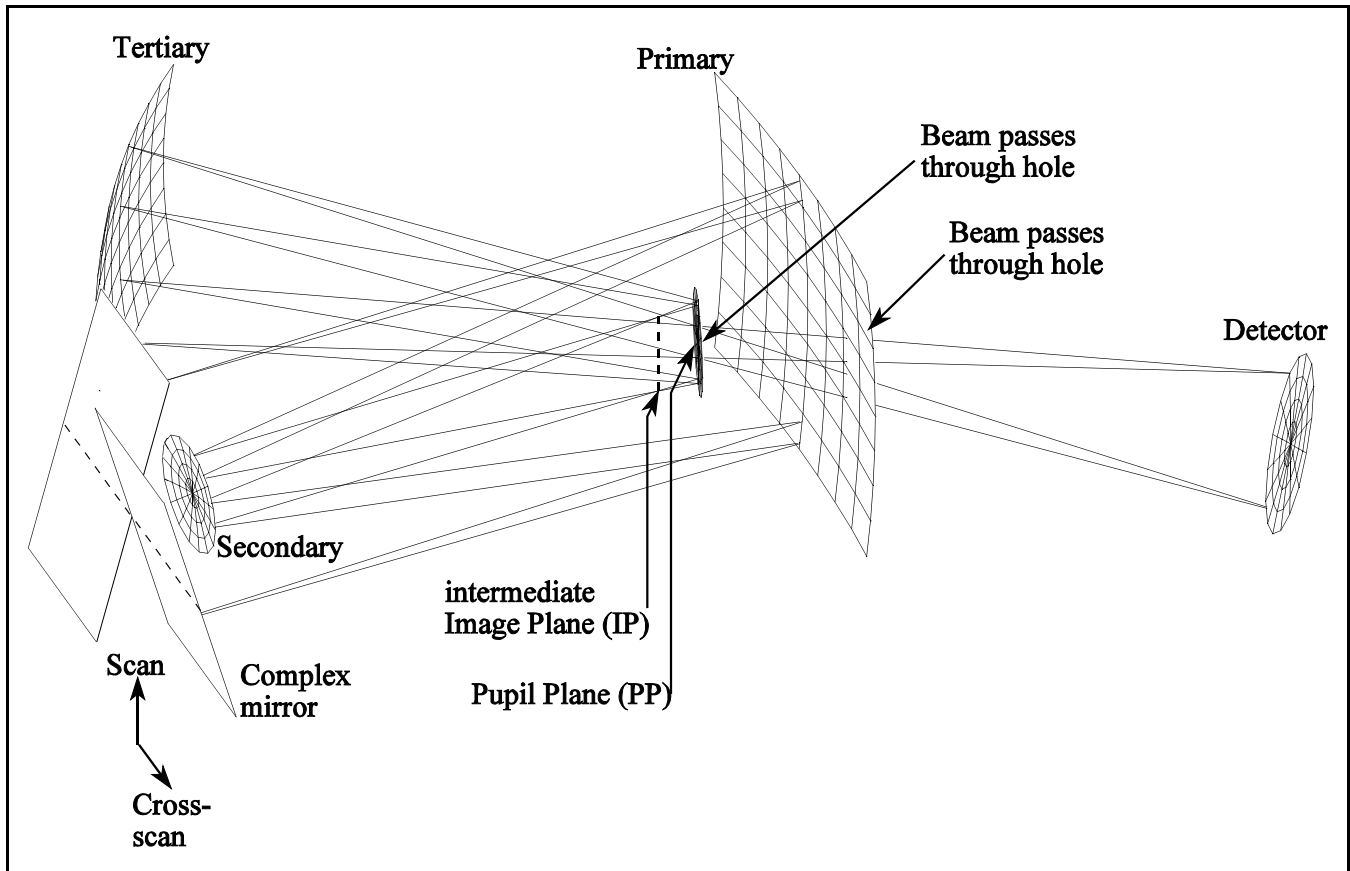


**Figure 2.** Layout diagram for system with 7.5 m focal length. The complex mirror gives the primary two look directions separated in the scan direction by  $\sim 1$  radian or more. The primary has an off-center hole for the beam from tertiary to detector. Additional portions of a central stripe (along the cross-scan direction) would not receive useful light because of obscuration by the secondary and fold.

perhaps the optical element most likely to warp or shift position thermally, and if it is made the stop, light from all parts of the field will experience the same effect.

In order to define the aperture completely, the stop must have a central obscuration to block light which would otherwise be blocked by the secondary. To minimize the required size of this central obscuration and to facilitate mounting, the secondary should be placed near the complex mirror, probably mounted on it (and possibly moved slightly behind it to facilitate baffling). The complex mirror should also be far enough from the primary so that with the incoming beams separated by the basic angle there is no beam blockage by the primary. For the case of the complex mirror near the secondary, as shown in Fig. 2, the basic angle must be at least  $58^\circ$  for the incoming beam to clear the primary.

We and others have considered the use of a prism to obtain spectral information. (See, for example, Röser, *et al.*<sup>4</sup>) A prism also enhances the information return on bright stars, via the enhanced visibility, but our sensitivity calculations show that the effect is fairly small, particularly with the short-focal-length approach envisioned here. A prism has the obvious potential to introduce systematic error. Fortunately, as discussed in the previous section, our recent simulations have shown that the star's temperature can be determined without the use of a prism.

To treat beam blockage, it is useful to simplify the drawing by eliminating all the folding mirrors, with the primary, secondary, tertiary, and detector unchanged (Fig. 3). This "non-folded" drawing has a single optical axis. To avoid vignetting, rays are blocked either at the pupil or an image of the pupil, or at an image of the field. These blockages will be treated below in order from the entrance of light into the instrument to the detector:

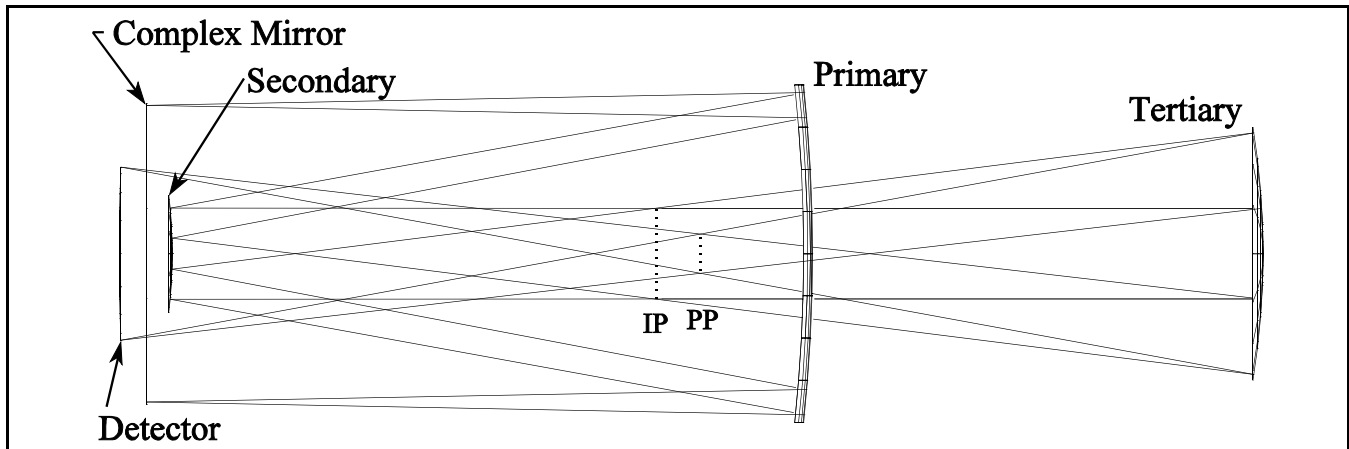


**Figure 3.** Non-folded drawing of the design of Fig. 2, for illustrating beam clearance. IP is the image plane following the secondary, and PP is the pupil plane following the tertiary.

- a) The secondary blocks the beam at the complex mirror. The aperture must have a central obscuration to avoid vignetting.
- b) The beam from primary to secondary is blocked by the fold near the image plane. This requires a central obscuration in the aperture that is larger than that for blockage (a). It is circular, 0.25 m in diameter.
- c) In Fig. 3, the beam from secondary to tertiary would need to pass through the primary. This would require a hole that in turn would require enlarging the central obscuration at the complex mirror, but not in the folding scheme adopted (Fig. 2).
- d) On the way from tertiary to detector, the beam must again pass through the primary, and this time the problem is not avoided by the chosen folding scheme. However, the fold mirror tilts the beam in the cross-scan direction (see Fig. 2), so the required hole in the primary and obscuration at the complex mirror fall in a central stripe carrying little astrometric information.
- e) Finally, and this blockage is the most serious, in Fig. 3 the beam from tertiary to detector must also pass the secondary, or if the detector is to the right of the secondary, the beams from primary to secondary and secondary to IP must clear the detector. This potential blockage is why the folding scheme shown, or an equivalent, is needed. The single fold mirror may be placed in either of two positions: 1) (the scheme adopted) in the secondary-to-tertiary beam, near the image plane (IP) and coincident with the pupil plane (PP) that exists in the beam returning from the tertiary; or 2) (an alternate scheme) in that returning beam, at the PP. In either case, the unusable portion can be directed with another mirror to another instrument, for multiband photometry or examination with a different EFFL, for example.

#### 4. TECHNIQUE FOR MAPPING THE PARAMETER SPACE

The general description of a three-mirror optical system in the paraxial approximation requires seven parameters: the radii of curvature of three mirrors plus the detector,<sup>f</sup> and three "thicknesses" (the distance from each powered element to the next) (Table 2). (The case of a flat detector surface is considered.) These parameters are labeled  $\{R_i, t_j\}$ , where  $i=1, \dots, 4$  and  $j=1, 2, 3$ . To reduce aberration, each of the three powered mirrors is also given three additional adjustable coefficients in the expression for the height of the surface.<sup>g</sup> They are conic constant,<sup>h</sup> and coefficients of  $\rho^6$  and  $\rho^8$ . The higher order terms add 9 quantities to be adjusted, making 16 in all. Aberration can be reduced, albeit at the expense of manufacturing complexity,

<sup>f</sup> Flat detector chips may be mounted on facets of a polyhedral detector surface to approximate a curved image plane. This improves performance, but adds complexity.

<sup>g</sup> The surface height is defined as its departure along the optical axis from a plane.

<sup>h</sup> The conic constant multiplies terms in the height of order  $\rho^4$  and higher, where  $\rho$  is radius from the optical axis.

**Table 2.** Optical parameters. “Abscissa” and “ordinate” refer to Fig. 4.

Sym	Element	Quantity	Status
$R_1$	Primary	Radius of Curv	Abscissa
$t_1$	Primary	Spacing	Ordinate
$R_2$	Secondary	Radius of Curv	Optimized $\ni$ blur min.
$t_2$	Secondary	Spacing	Optimized $\ni$ 0 distortion
$R_3$	Tertiary	Radius of Curv	Solve: EFFL
$t_3$	Tertiary	Spacing	Solve: paraxial focus
$R_{det}$	Detector	Radius of Curv	Free parameter

by adding correction terms (but not optical power) on the complex mirror. However, the height distribution associated with these terms must be stretched to an elliptical distribution.<sup>5</sup> This was not investigated here.

The optical optimization minimizes a merit function comprising terms representing blur (geometrical aberration) and image distortion, plus some terms included to constrain the design to be physically sensible. In principle, one could put all the requirements and desiderata into the merit function, allow the optimizer to adjust all 16 quantities, and wait for the ideal solution to appear. There are two problems with this approach. One is that there are at least these three desiderata: that the aberration be small, that the optics fit in the spacecraft package, and that the beam blockage be small. Each preference is met, more or less, by a wide variety of designs, but not all three simultaneously. A balance among them must be struck.

This cannot reasonably be coded into the merit function until the trades are understood. The other problem is that, when given too many variables to adjust at once, the optimizers tend to locate elements at infinity, or to make other ridiculous choices. A large number of constraints must be added to prevent this. We needed a better mousetrap.

The number of the lowest-order parameters  $\{R_i, t_j\}$  that were under optimizer control had to be reduced (see Table 2). A constraint on  $t_3$  is provided by requiring that the detector be at the paraxial focus, which is not necessarily optimum but perfectly adequate. A constraint on a combination of parameters is provided by requiring that the effective focal length match the desired value. These constraints are implemented as "solves," so there are two fewer independent variables. Detector curvature is another constraint; since it is a parameter of the optical model, it can simply be set. It must be moderate, as the individual detector chips are flat. We determined performance for several discrete values of EFFL and detector curvature, and the achievable performance will be a guide in choosing final values. This leaves 4 of  $\{R_i, t_j\}$  to be varied under the optimizer’s control.

In principle, two more lowest-order parameters could be eliminated. Meeting the aberration requirement requires that the Petzval sum (the sum of surface curvatures) be approximately equal to the curvature of the detector, but this condition is difficult to implement with a solve in Zemax<sup>6</sup>, the optical design program we used, or with any similar mechanism. Therefore, we count on the merit function operands describing blur to drive the Petzval sum to the correct value. Distortion is required to be very nearly zero, and can be made zero by acceptable parameter adjustments. An analytic expression for distortion exists, but it would be difficult to implement. Therefore, an operand is included in the merit function for distortion, and it drives the distortion toward zero.

Finally, with  $R_1$  and  $t_1$  fixed, the optimization is sufficiently constrained to converge well. Adequate designs can be found for many choices of  $R_1$  and  $t_1$ . To present a clear picture of the trades among the three desiderata, we optimized designs automatically over ranges of  $R_1$  and  $t_1$ , and made contour plots of the three desiderata. Plots were made for ranges of these parameters (Fig. 4). These plots were repeated for several values of EFFL and detector curvature. This approach yielded a graphic representation of the three desiderata as functions of four independent variables. Performance of one example system from each combination of EFFL and detector curvature is summarized in Table 3.

The rays traced in the optimizations were spread uniformly over the aperture, with the central obscuration modeled. Each merit function evaluation involved tracing 2200 rays through the system. This number was used to achieve a moderately accurate representation of the rectangular aperture, at a range of field angles (employing bilateral symmetry in the cross-scan direction). The optimizations for Fig. 4, and the other four cases, each required about 20 hours on a 200 MHz workstation.

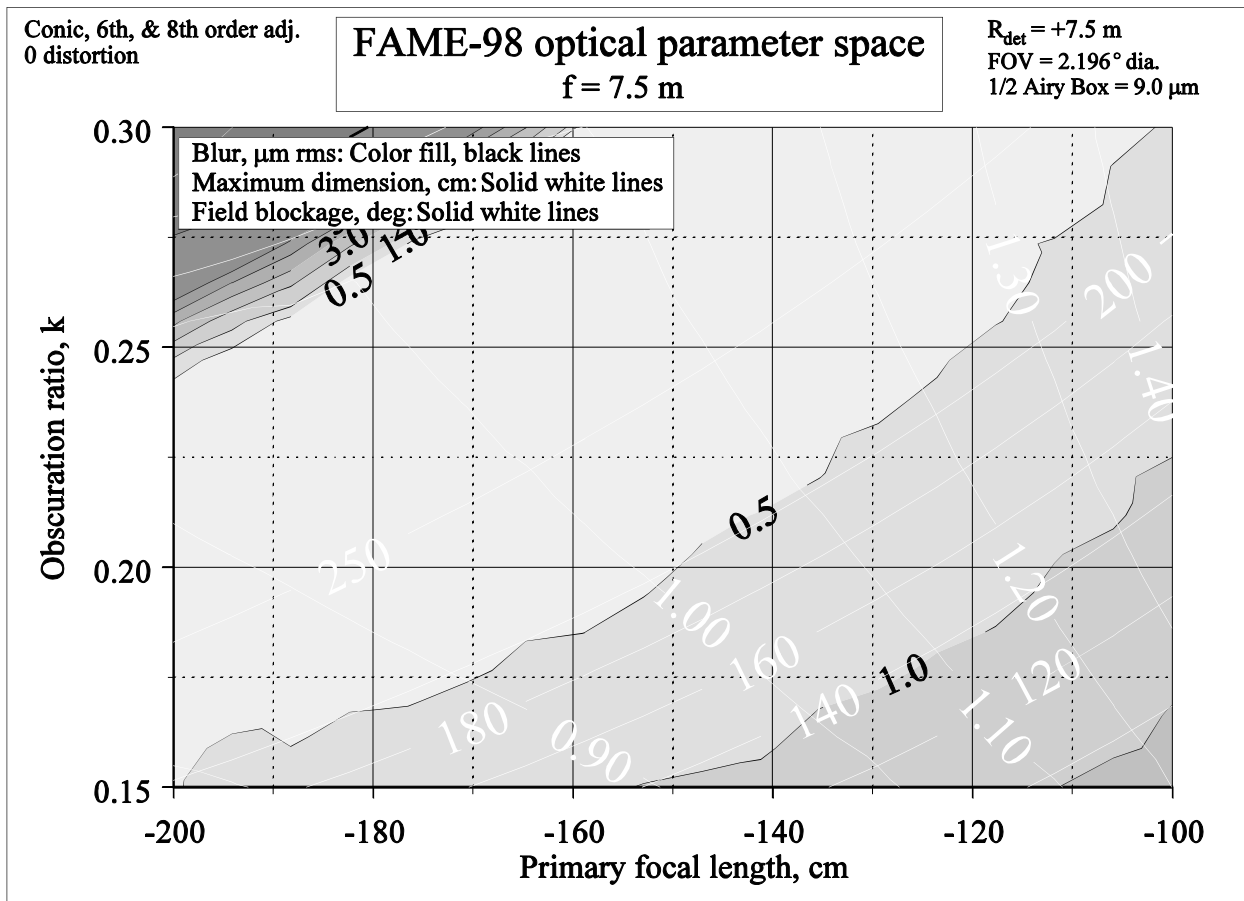


**Figure 4.** Parameter space diagram for EFFL = 7.5 m,  $R_{\text{det}} = +7.5 \text{ m}$ . The abscissa is the focal length of the primary,  $f_1 = 2/R_1$ . The ordinate is the secondary "obscuration ratio", the ratio of the diameter of the secondary to that of the primary,  $k = 1 - t_1/f_1$ , where  $t_1$  is the primary-secondary spacing.

This design form and method may also be applicable to FAME-96 with its EFFL of 36 m. A preliminary investigation gave promising results. A future study could investigate further, if interest in a design with a longer EFFL is revived.

**Table 3.** Candidate designs, vs. focal length and detector radius of curvature.

EFFL m	$R_{\text{det}}$ m	blur*, μm rms	FOV(min)** , deg	FOV(max) radius, deg	$2f\lambda_0/S$ μm	Comments
5.	+7.5	1.541	0.818	1.647	12.0	beam clearance difficult
6.25	+7.5	0.856	0.658	1.317	15.0	
7.5	+7.5	0.796	0.545	1.098	18.0	nominal; optical diagram is Fig. 2
10.	+7.5	0.423	0.410	0.823	24.0	
6.25	∞	0.783	0.648	1.317	15.0	beam clearance difficult (see text)

\* rms is over both field and pupil.

\*\* This is half the side length of a square blockage.

## 5. RESULTS

The contour map of performance for designs with 7.5 m focal length and a detector with +7.5 m radius of curvature is shown in Fig. 4. The blur has a wide trough-shaped minimum running from lower left to upper right. Image quality in the trough is excellent: rms blur is under  $0.5 \mu\text{m}$ ,  $1/18$  of the half-width of the Airy box ( $\lambda_0/S$ ). The trough becomes substantially wider and deeper as EFFL is increased.

As described above, we can trade away some of this image quality to meet other criteria. Contours of constant physical size ("maximum dimension") are roughly parallel to those of constant blur, but the system size increases monotonically from lower right to upper left. Working on the lower right side of the trough, the two parameters vary together. Fortunately, there exists a region below and to the right of the floor of the trough in which size and blur are both acceptable. Contours of constant field blockage ("min. usable field radius") are nearly at right angles to the blur and size contours, showing that less blockage with the same blur and size can be had by moving along the blur and size contours, to the lower left. The contour-map approach has revealed the generalities of the choice in the parameter spaces mapped, and leaves the designer free to consider other factors, such as additional packaging constraints.

The systems grow very large at the upper left of the diagrams, and an arbitrary limit on size was imposed via the merit function, to prevent runaway solutions. This accounts for the appearance of a "wall" in the blur contours in this region. Because the upper left region contains systems that are too large to be useful, it was not investigated further.

For this paper, point designs for each combination of EFFL and detector curvature studied were selected from the applicable map with a maximum system size of 1.8 m, and with the side length of the (square) field blockage equal to half the field diameter, i.e., a loss of  $1/\pi$  of the field area. Parameter values and performance measures for the five example designs are given in Table 3, and the corresponding optical prescriptions are given in Table 4. The slopes of the departure of the aspheric surfaces from the best-fit sphere are all well within current limits on manufacture.

The blur achieved in the systems of Table 3 improves quite rapidly as one goes to longer focal length. Furthermore, for a focal length of 5 m, an additional circular beam blockage arises at the primary, leaving only an outer rim, 57% of the total area, usable. This design may actually be viable, but at this conceptual stage, we decided to adopt a focal length that did not impose strong constraints on the optical design, so we adopted a focal length of 7.5 m, leaving global optimization for later. This design is illustrated in Figs. 2-3. The rms blur is  $0.8 \mu\text{m}$  and the average wavefront error (WFE) is  $0.05 \mu\text{m}$  peak to valley, along the same arc as the spot diagram (Fig. 5). This is likely to be less than the WFE introduced by even state-of-the-art manufacturing and alignment errors.

**Table 4. Optical Prescriptions.** Units for columns of radius of curvature ( $R_i$ ) and thickness ( $t_i$ ) are m. Conic constants ( $\kappa_i$ ) are dimensionless. Positive curvature means concave.

EFFL m	Primary			Secondary			Tertiary			Det.
	$R_1$	$t_1$	$\kappa_1$	$R_2$	$t_2$	$\kappa_2$	$R_3$	$t_3$	$\kappa_3$	$R_4$
5.	2.480	0.983	-0.916	-0.850	0.648	-4.002	1.423	1.847	-0.295	7.50
6.25	2.560	1.014	-0.937	-0.833	0.738	-3.622	1.350	1.864	-0.348	7.50
7.5	2.660	1.057	-0.950	-0.823	0.808	-3.388	1.302	1.889	-0.392	7.50
10.	2.830	1.135	-0.965	-0.808	0.913	-3.103	1.229	1.947	-0.457	7.50
6.25	3.650	1.551	-0.915	-1.109	0.541	-6.464	1.597	2.183	-0.273	$\infty$

### 5.1. Chosen design: EFFL = 7.5 m, curved detector.

A spot diagram for the nominal design, with EFFL = 7.5 m, is shown in Fig. 5. As one would expect, spots at the extremes of the field do appear noticeably worse than those shown. The overall performance is reflected in the rms spot size (of  $0.8 \mu\text{m}$ ) in Table 3, in which the rms extends over both field and pupil. The blur turns up sharply at the field edge, so it

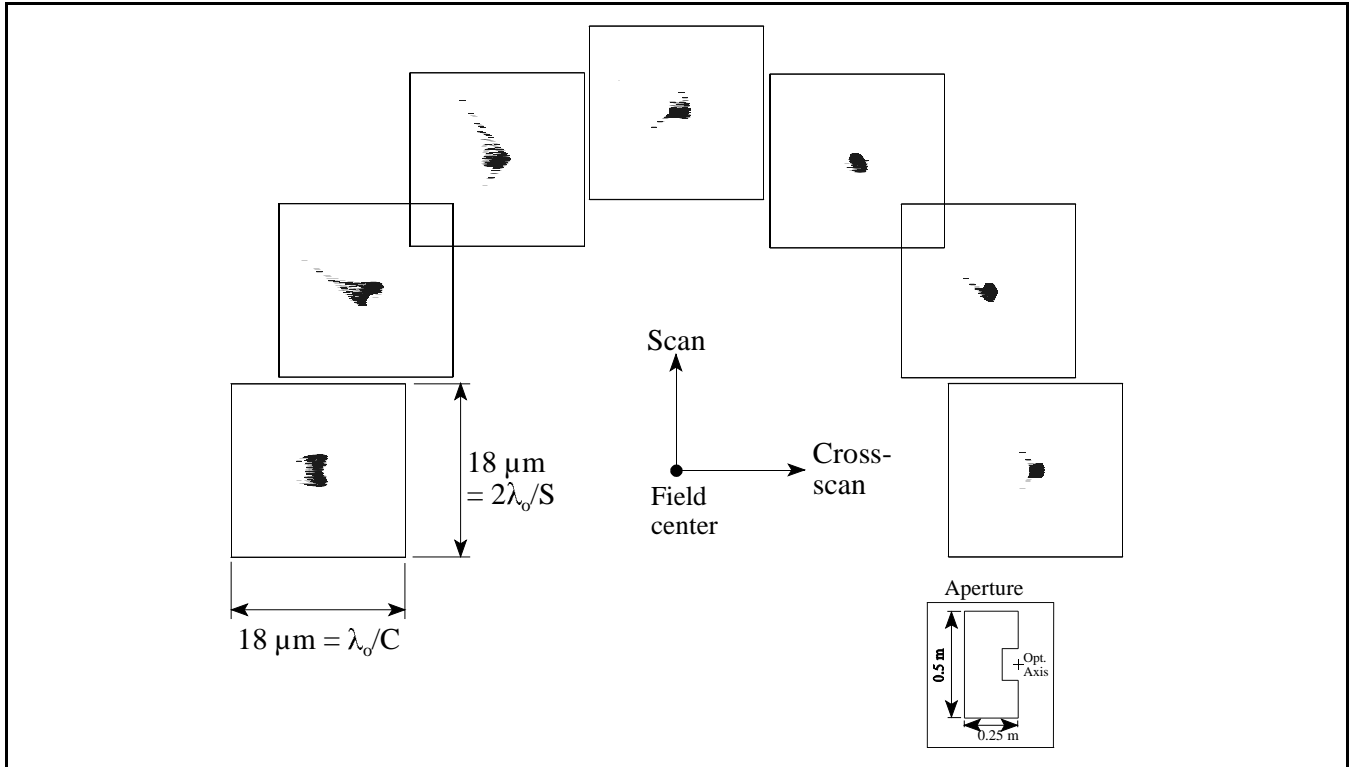


**Figure 5.** Spot diagram for nominal design (EFFL = 7.5 m), for points along an arc as shown, at a field angle  $1.03^\circ$  from the center. (The edge of the field is at a radius of  $1.1^\circ$ .) Rms spot size along this arc matches the rms over the whole field. Boxes shown are one Airy box in the scan direction by one-half Airy box in the cross-scan direction. (Light from the center of the field cannot reach the detector array because of blockage by the fold mirror. The field is bounded on the inside by a square of side  $1.1^\circ$ .) There is bilateral symmetry in the scan direction, so the spot diagrams for field points at negative scan angles can be obtained by reflecting points shown across a horizontal line. The inset shows the shape of the aperture along one of the two look directions. The shape is that of one of the halves of the complex mirror, with an obscuration so that light headed for the primary does not strike the secondary. A peculiarity of the drawing software is that individual ray intercepts are drawn here as short horizontal dashes.

would probably be possible to reduce the maximum blur across the desired field by broadening the field area over which the optimizations are done, accepting worse blur at intermediate field radii, but obtaining better at the edges of the desired field. A decision to make such a change might follow the detailed layout of detector chips in the focal plane.

## 5.2. Flat detector case.

With a flat detector, blur and maximum size are nearly the same as with the curved detector, but for a given primary focal length and secondary obscuration ratio ( $f_1$  and  $k$ ), the field blockage is substantially larger. A flat detector would make the system simpler, so it is worth some trouble, expense, or loss of throughput to achieve. We studied in detail the possibility of a flat detector with EFFL = 6.25 m, and found it problematic. Using the system selected as described above from the map, there are beam blockage problems associated with the fold, whether it is placed at the IP or at the PP. Using instead a system located nearer the center of the ( $f_1$ ,  $k$ ) region mapped, field blockage is much more severe than for a curved detector. It is left as the subject of a future study to determine the extent to which a satisfactory system can be worked out, and the range of EFFL for which such satisfactory systems exist.

Alternatively, one could consider a refractive field flattener as in the DIVA design<sup>1</sup>, although it would create the obvious problem of thermal variation of index of refraction. We have not seen a way to add a reflective field flattener to this system as was possible with FAME-96, but we have not looked exhaustively. Reducing aberration with a reflective corrector

on the complex mirror (having no spherical power) would give greater freedom elsewhere and might help solve this beam clearance problem, at a price in manufacturing complexity.

This leaves us with a trade. For the added complexity of a curved focal plane we can have additional space to put detectors (if the cost of the added devices, support electronics, on-board processing, telecom, and ground-based analysis is not prohibitive). For now, we take the curved detector plane as the nominal.

### 5.3. Beam propagation within the detector.

The designs discussed in this paper are not telecentric, so at the periphery of the field, the beam impinges on the detector at a substantial angle. The depth to which photons penetrate before they are converted to electric charge is a strong function of wavelength, from  $\ll 1 \mu\text{m}$  at 400 nm to 10's of  $\mu\text{m}$  at 900 nm (at 200°K). Thus, the near-infrared light will penetrate further than the visible and, if it is not traveling at right angles to the surface of the chip, will be absorbed in a different place. This effect yields a position bias that depended on the star's color. However, an ameliorating factor is that due to silicon's high index of refraction, the angle between the propagation direction and the normal to the surface of the chip will be reduced a factor of about 4 as it enters. (The ameliorating factor also depends on star color, due to the wavelength dependence of silicon's index of refraction.) This bias can be modeled as a function of field position and star color. Thus, to the extent that the star's color is known, the bias can be removed in the data analysis.

## 6. ACKNOWLEDGMENTS

This work has been supported by the U.S. Naval Observatory and the Smithsonian Institution. We gratefully acknowledge helpful conversations with J. Baker, H. Epps, and W. McKinley, and thank P.K. Seidelmann and M.A. Murison for thoughtfully reviewing the manuscript.

## 7. REFERENCES

1. E. Høg, C. Fabricius, and V.V. Makarov, "Astrometry from Space: New Design of the GAIA Mission", *Experimental Astronomy*, **7**: 101-115 (1997). The DIVA design is a prototype for GAIA.
2. R.D. Reasenberg and J.D. Phillips, "Design of a Spaceborne Astrometric Survey Instrument", paper 3356-38 in these proceedings. The study of the influence of aperture shape on mission throughput discussed therein is for bright stars, for which detector read noise can be ignored.
3. "The Hipparcos Mission: Pre-Launch Status", vol. 1: "The Hipparcos satellite", ESA SP-1111 (June 1989). (Launch was in August 1989.)
4. S. Röser, U. Bastian, K.S. de Boer, E. Høg, H.P. Röser, C. Schalinski, E. Schilbach, C. de Vegt, S. Wagner, "DIVA – Towards Microarcsecond Global Astrometry", Proceedings from the Hipparcos Venice '97 Symposium, Venice, May (13-16) 1997, available at <http://astro.estec.esa.nl/Hipparcos/venice.html#session12>.
5. D.J. Schroeder, *Appl. Opt.* **17**, 141 (1978). Also SP-1111, *op cit*, pp. 66-71. For Hipparcos, elliptically-shaped zones on the correcting plate were approximated by manufacturing circular zones, and removing and discarding a central stripe of the mirror. Note that SP-1111 also states that the coatings for Hipparcos' beam combiner, primary, and fold flat were Ag on a Cr adhesion layer, overcoated with ThF<sub>4</sub>.
6. TM, Focus Software, Tucson, AZ. This information is included for technical communication only, and is not intended as an endorsement.